

The Astronomical Journal, submitted 10/27/1999

**The velocity and mass distribution of clusters of galaxies
from the CNOC1 cluster redshift survey**

Roeland P. van der Marel

Space Telescope Science Institute, 3700 San Martin Drive, Baltimore, MD 21218

John Magorrian

Institute of Astronomy, Madingley Road, Cambridge CB3 0HA, United Kingdom

Ray G. Carlberg, H. K. C. Yee

Department of Astronomy, University of Toronto, Toronto ON, M5S 1A7, Canada

E. Ellingson

Center for Astrophysics & Space Astronomy, University of Colorado, Boulder, CO 80309-0389

arXiv:astro-ph/9910494v2 24 Jan 2000

ABSTRACT

In the context of the CNOC1 cluster survey, redshifts were obtained for galaxies in 16 clusters. The resulting sample is ideally suited for an analysis of the internal velocity and mass distribution of clusters. Previous analyses of this dataset used the Jeans equation to model the projected velocity dispersion profile. However, the results of such an analysis always yield a strong degeneracy between the mass density profile and the velocity dispersion anisotropy profile. Here we analyze the full (R, v) dataset of galaxy positions and velocities in an attempt to break this degeneracy.

We build an ‘ensemble cluster’ from the individual clusters under the assumption that they form a homologous sequence; if clusters are not homologous then our results are probably still valid in an average sense. To interpret the data we study a one-parameter family of spherical models with different constant velocity dispersion anisotropy, chosen to all provide the same acceptable fit to the projected velocity dispersion profile. The best-fit model is sought using a variety of statistics, including the likelihood of the dataset, and the shape and Gauss-Hermite moments of the grand-total velocity histogram. The confidence regions and goodness-of-fit for the best-fit model are determined using Monte-Carlo simulations. Although the results of our analysis depend slightly on which statistic is used to judge the models, all statistics agree that the best-fit model is close to isotropic. For none of the statistics does the $1\text{-}\sigma$ confidence region extend below $\sigma_r/\sigma_t = 0.74$, or above $\sigma_r/\sigma_t = 1.05$. This result derives primarily from the fact that the observed grand-total velocity histogram is close to Gaussian, which is not expected to be the case for a strongly anisotropic model.

The best-fitting models have a mass-to-number-density ratio that is approximately independent of radius over the range constrained by the data. They also have a mass-density profile that is consistent with the dark matter halo profile advocated by Navarro, Frenk & White, in terms of both the profile shape and the characteristic scale length. This adds important new weight to the evidence that clusters do indeed follow this proposed universal mass density profile.

We present a detailed discussion of a number of possible uncertainties in our analysis, including our treatment of interlopers and brightest cluster galaxies, our use of a restricted one-parameter family of distribution functions, our use of spherical models for what is in reality an ensemble of non-spherical clusters, and our assumption that clusters form a homologous set. These issues all constitute important approximations in our analysis. However, none of the tests that we have done indicates that these approximations influence our results at a significant level.

Subject headings: dark matter — galaxies: clusters: general — galaxies: kinematics and dynamics.

1. Introduction

Determinations of the internal velocity and mass distribution of galaxy clusters are of great value, since they have the potential to constrain both the main cosmological parameters and scenarios for large-scale structure formation (e.g., Crone, Evrard & Richstone 1994; Cole & Lacey 1996; de Theije, van Kampen & Slijkhuis 1998, 1999). A recent development on this problem has been the prediction from cosmological simulations that dark matter halos have a universal density profile (Navarro, Frenk & White 1997; hereafter NFW). Testing the validity of this prediction is an important goal for any study of cluster structure. The traditional way to study these issues is to construct dynamical equilibrium models for the redshift measurements of individual cluster galaxies. Alternative approaches to infer the mass distribution of clusters are to use X-ray observations (e.g., Allen 1998; Hughes 1998), measurements of the weak- or strong-lensing of background sources (e.g., Bartelmann & Narayan 1995), or caustics in redshift space (Geller, Diaferio & Kurtz 1999; Diaferio 1999). Each of the different methods has its own uncertainties and biases, and results from different methods are often found to differ. The causes and magnitudes of these differences remain a hot topic of debate (e.g., Lewis et al. 1999 and references therein).

Here we focus attention on the dynamical analysis of galaxy redshifts.¹ Analyses of this type have nearly always been restricted to modeling of the projected velocity dispersion profile $\sigma(R)$ (e.g., Kent & Gunn 1982; Merritt 1987), often using the Jeans equation (e.g., Solanes & Salavdor-Sole 1990; den Hartog & Katgert 1996; Natarajan & Kneib 1996). The main limitation of such analyses is that there are two unknown functions of one variable, the mass density profile $\rho(r)$ and the velocity dispersion anisotropy profile $\beta(r)$, that are both constrained by only one function of one variable, $\sigma(R)$. As a result, there is always a degenerate set of models with different $\rho(r)$ and $\beta(r)$ that can all fit the observations equally well (Binney & Mamon 1982). Attempts are often made to break this degeneracy by assuming that either one of $\rho(r)$ or $\beta(r)$ is known, so that the other can be determined. Popular assumptions are that the velocity distribution is isotropic, or that the mass distribution can be calculated from the observed number density by the assumption of a constant mass-to-number density (or mass-to-light) ratio. However, neither of these assumptions has a strong physical justification, so these approaches do not remove the underlying degeneracy.

As a result of steady improvements in instrumentation, and in particular the advent of efficient multi-object spectrographs, the available redshift samples for galaxy clusters have been steadily increasing in size. Important recent datasets are the ENACS (ESO Nearby Abell Cluster Survey) (e.g., Katgert et al. 1996) and the CNOC1 (Canadian Network for Observational Cosmology) cluster redshift survey² (e.g., Yee, Ellingson & Carlberg 1996). With improved statistics it should

¹Dynamical models of clusters of galaxies based on the Boltzmann equation (or its integrals, the Jeans equations and the virial theorem) always assume implicitly that the system is in equilibrium. While this is not strictly true for a cluster of galaxies, numerical simulations show that cluster evolution proceeds through a series of quasi-equilibrium states that satisfy the Boltzmann equation in an approximate sense (Natarajan, Hjorth, & van Kampen 1997).

²We refer to the CNOC cluster redshift survey as ‘CNOC1’, to distinguish it from the subsequent CNOC2 field galaxy redshift survey (e.g., Lin et al. 1999).

become possible to extract not only velocity dispersion profiles from the data, but also higher order moments that describe deviations of the observed velocity histograms from a Gaussian shape (Zabludoff, Franx & Geller 1993). Such measurements have the potential to break the degeneracy between the mass and velocity distribution, as emphasized in this context by, e.g., Merritt (1987; 1993) and Merritt & Saha (1993).

Here we focus on the data from the CNOC1 cluster survey. Redshifts were obtained for galaxies in 16 clusters at $z = 0.17\text{--}0.55$, selected on the basis of their X-ray luminosity. Previous analyses of these data were all based either on use of the virial theorem (Carlberg et al. 1996; hereafter C96) or the Jeans equation (Carlberg et al. 1997a,b,c; hereafter C97a,b,c). These analyses yielded the important result that if cluster of galaxies have a velocity distribution that is not too far from isotropic, then the CNOC1 data are consistent with clusters having an approximately constant mass-to-number-density ratio, and a mass-density profile that is approximately of the NFW form with a scale radius that is consistent with predictions from cosmological simulations. However, because of the degeneracy intrinsic to the Jeans equation, models with significant anisotropies and very different mass profiles can fit the projected velocity dispersion profile equally well. So the important question is: can the range of allowed models for the CNOC1 data be reduced by considering not only the projected velocity dispersion profile, but also the entire (R, v) dataset and the implied higher-order velocity moments? This question is the main topic of the present paper. To answer it, we present a new analysis of the CNOC1 dataset, in part similar in spirit to that suggested by Merritt & Saha (1993), but with some differences (see §4.2 below).

In §2 we first repeat some of the Jeans modeling of $\sigma(R)$, but using a different approach from that employed by C97a,b,c. The results not only provide an illustration of the degeneracies involved in the modeling, but also serve as a useful starting point for the more detailed analysis. In §3 we analyze the full (R, v) dataset. We seek a best-fit model using a variety of statistics, including the likelihood of the dataset and the shape and Gauss-Hermite moments of the grand-total velocity histogram. The confidence regions and goodness-of-fit for the best-fit model are estimated using Monte-Carlo simulations. In §4 we discuss possible uncertainties in our analysis, and how robust the conclusions of our analysis are in view of these uncertainties. In §5 we present and discuss the final conclusions. In Appendix A we compare our modeling approach to that of Ramirez & De Souza (1998) and Ramirez, De Souza & Schade (1999), who recently used a more approximate method to constrain the orbital anisotropy of cluster galaxies from observed cluster velocity histograms (including that for the CNOC1 sample).

2. Jeans equation models

In the CNOC1 cluster survey redshifts were obtained for galaxies in 16 different clusters. The characteristic size and velocity of each cluster can be quantified by, e.g., the radius r_{200} inside which the average mass density equals 200 times the critical density of the Universe (at the given redshift), and the line-of-sight velocity dispersion σ . For our dynamical analysis we treat the data similarly as in C97b: we assume that clusters form a homologous sequence, each with identical

structure in dimensionless units. To study this dimensionless structure we consider the dataset that contains for each galaxy in the survey the quantities $\tilde{R} \equiv R/r_{200}$ and $\tilde{v} \equiv v/\sigma$, where R is the projected distance from the cluster center, v is the observed line-of-sight velocity with respect to the systemic cluster velocity, and r_{200} and σ are taken from the analysis of C97b. One may consider the (\tilde{R}, \tilde{v}) as quantities drawn from ‘the ensemble cluster’. The advantage of combining data from different clusters is that it reduces the influence of, e.g., substructure and non-sphericity on the properties of the dataset. With this approach, spherical equilibrium models are likely to provide an adequate description of the data (see §4.4 and §4.5 below).

Hereafter we write (R, v) instead of (\tilde{R}, \tilde{v}) , with the understanding that all quantities discussed are dimensionless unless otherwise noted. In our dynamical analysis we also work in dimensionless units. To this end we adopt a unit of mass

$$M_{\text{u}} = (2.3252 \times 10^{14} M_{\odot}) (r_{200}/\text{Mpc}) (\sigma/[10^3 \text{ km s}^{-1}])^2 \quad (1)$$

chosen to set the gravitational constant to $G = 1$.

The projected galaxy number density profile $\Sigma(R)$ of the CNOC1 ensemble cluster was derived in C97b, with corrections for both the non-uniform sampling of the clusters (see Yee et al. 1996) and interloper contamination. Figure 1 shows the result; Σ is the number of galaxies per unit area with K-corrected absolute Gunn r -band magnitude $M_r < -18.5$,³ normalized to unity over the circular region with radius r_{200} . For the dynamical modeling we have fitted to the data a smooth function of the form

$$\Sigma(R) = \Sigma_b 2^{\frac{\beta-\gamma}{\alpha}} (R/b)^{-\gamma} [1 + (R/b)^{\alpha}]^{-\frac{\beta-\gamma}{\alpha}} [1 + (R/c)^{\delta}]^{-\frac{\epsilon-\beta}{\delta}}. \quad (2)$$

This somewhat arbitrary parameterization is similar to the ‘nuker-law’ advocated by, e.g., Byun et al. (1996), but is more general in having two power-law breaks rather than one. A good fit was obtained with $\Sigma_b = 1.03$, $b = 0.21$, $c = 1.32$, $\alpha = 2.97$, $\beta = 1.51$, $\gamma = 0.65$, $\delta = 4.00$, and $\epsilon = 3.00$. The parameterized fit is shown in Figure 1. The fit to the data is statistically acceptable, but note that the fit is not unique; the parameters of equation (2) are strongly correlated, and are not all equally well constrained. C97c showed that the projection of a profile such as that advocated by NFW also provides an acceptable fit to the data.

To interpret the dynamics of the ensemble cluster we first model the projected velocity dispersion profile using the Jeans equation for a spherical system. The software used for this was similar to that discussed in van der Marel (1994). The intrinsic galaxy number density profile $\nu(r)$ follows from the projected galaxy number density profile $\Sigma(R)$ by solution of the relevant Abel transform equation. An ansatz is made for the mass density profile $\rho(r)$ of the cluster, and from this the gravitational potential and gravitational force are calculated. The Jeans equation is then solved for the intrinsic velocity dispersions of the system (the tangential velocity dispersion $\sigma_t = \sigma_{\theta} = \sigma_{\phi}$ and the radial velocity dispersion σ_r), for some velocity dispersion anisotropy profile $\beta(r)$, where $\beta \equiv 1 - \sigma_t^2/\sigma_r^2$. The intrinsic velocity dispersion components in the direction to the

³The value of the absolute magnitude limit assumes a Hubble constant $H_0 = 100 \text{ km s}^{-1} \text{ Mpc}^{-1}$. This is the only quantity in this paper that depends on H_0 , because our entire analysis is performed in dimensionless units.

observer are then weighted with the intrinsic galaxy number density and projected along the line of sight to yield the projected line-of-sight velocity dispersion profile $\sigma(R)$, which can be compared to observations.

As discussed in §1, there is always a degenerate set of models with different $\rho(r)$ and $\beta(r)$ that all fit $\sigma(R)$ equally well. The goal of the present paper is to see to what extent this degeneracy can be broken by modeling not only the projected velocity dispersion profile, but also the individual (R, v) data points (and thus indirectly the higher order velocity moments). We do not wish to be too ambitious and therefore restrict ourselves to a one-parameter family of models, namely those in which the velocity dispersion anisotropy is independent of radius, $\beta(r) = \text{constant}$. There is a unique mass density profile $\rho(r)$ for each constant β , such that models with different β all provide an identical fit to the observations. Instead of attempting to infer non-parametrically the optimum $\rho(r)$ for each β , we adopt a simple three-parameter family of models among which we seek the one that fits best. We set

$$\rho(r) = \rho_0 (r/a)^{-\xi} [1 + (r/a)]^{\xi-3}. \quad (3)$$

The parameters ρ_0 and a set the scale of the mass distribution in density and length, while ξ is the logarithmic power-law slope near the center. For $\xi = 1$ this mass density is of the form advocated by NFW; for $\xi = 0$ the mass density has a homogeneous core.

The projected velocity dispersion profile $\sigma(R)$ of the CNOC1 ensemble cluster was derived in C97b, with appropriate correction for interloper contamination. The dispersion profile that we have used in our analysis was obtained with a similar but slightly updated treatment of the data, and is shown in Figure 2. The inferred profile is mildly different from that analyzed in C97b, but is equivalent in a statistical sense. Eleven constant- β models were constructed to interpret the data, with β chosen such that the ratio σ_r/σ_t was sampled logarithmically between 1/3 and 3. For each β we determined the $\rho(r)$ for which the model predictions best fit the data. To this end we used a grid in the (a, ξ) parameter space. For each (a, ξ) we calculated the shape of the predicted velocity dispersion profile, and the density normalization ρ_0 that yields the best fit to the observed velocity dispersion profile in a χ^2 sense. We then sought the minimum χ^2 over the (a, ξ) parameter space to find the best-fitting mass density profile $\rho(r)$ for the given β . The velocity dispersion profiles predicted by these best-fit models are shown as curves in Figure 2. Apart from their small radii behavior (where there are no strong constraints from the data) the model predictions are similar for the different values of β , as expected based on the degeneracy of the problem. The small differences between the various models are due to the fact that a parameterized form was used for the mass density $\rho(r)$; the true $\rho(r)$ that best fits the data may not be exactly of the adopted form. However, the fits to the data in Figure 2 are all statistically acceptable, as judged by the χ^2 of the fit. So even though a non-parameterized modeling approach would likely yield mass densities $\rho(r)$ that differ from the parameterized form adopted here, the differences would not be statistically significant. This provides a posteriori justification for the use of the adopted mass density parameterization.

Figure 3 shows the parameters ρ_0 , a and ξ of the best-fitting mass density $\rho(r)$ as a function of the anisotropy σ_r/σ_t . Solid dots indicate the models for which the predictions are shown in Figure 2. The profiles $\rho(r)$ for these models are shown in the top right panel of Figure 4. As the

value of σ_r/σ_t is increased, the scale radius a increases while the small radii slope ξ decreases. Consequently, tangentially anisotropic models have higher mass densities and steeper mass density profiles at small radii than radially anisotropic models. Very radially anisotropic models formally attain their best fit for $\xi < 0$, i.e., with decreasing mass densities near the center. This seems implausible for various reasons, and we therefore fixed $\xi = 0$ for these models. This has little effect on the quality of the fit to the observed velocity dispersion profile, cf. Figure 2.

The bottom right panel of Figure 4 shows the enclosed mass profile $M(r)$ for the models. The profile shapes depend strongly on the anisotropy, with tangentially anisotropic models being more centrally concentrated than radially anisotropic models. Interestingly, M_{200} , the enclosed mass within r_{200} ($\log(r) = 0$ in dimensionless units), is virtually independent of the assumed anisotropy.⁴ This was noticed previously by C97b, and significantly reduces the uncertainty in estimates of the cosmological mass density Ω from cluster mass-to-light ratios using Oort’s method.

The top left panel of Figure 4 shows the number density profile $\nu(r)$ of the models, as obtained by deprojection of the projected profile shown in Figure 1. When combined with the mass density profile $\rho(r)$ for each model one obtains the mass-to-number-density ratio $\rho/\nu(r)$, which is shown in the bottom left panel of Figure 4. This ratio decreases with radius for tangentially anisotropic models, and increases with radius for radially anisotropic models. The isotropic model (heavy curve) has a mass-to-number-density ratio $\rho/\nu(r)$ that is very nearly independent of radius. Note that the logarithmic slopes of the adopted $\nu(r)$ and $\rho(r)$ differ at asymptotically small and large radii (for $r \rightarrow 0$: $\nu(r) \propto r^{-1.65}$ and $\rho(r) \propto r^{-\xi}$; for $r \rightarrow \infty$: $\nu(r) \propto r^{-4}$ and $\rho(r) \propto r^{-3}$). So it is not an intrinsic property of the adopted parameterizations that isotropic models have approximately constant $\rho/\nu(r)$ over the region where this quantity is constrained by the data.

If the galaxy luminosity function of clusters is independent of position, then the mass-to-light ratio M/L is directly proportional to the mass-to-number-density ratio $\rho/\nu(r)$. In physical units, M/L is given by the dimensionless function $\rho/\nu(r)$ shown in Figure 4, multiplied by M_u/L_{200} . Here M_u is as given in equation (1), and L_{200} is the total luminosity inside a projected radius of r_{200} . The quantities r_{200} , σ and L_{200} for the individual clusters of the CNOC1 redshift survey are listed in Table 4 of C96 and Table 1 of C97b.

NFW have argued that cosmological simulations yield a more-or-less universal mass density profile $\rho(r)$ for dark matter halos, given by equation (3) with $\xi = 1$. Our models generate such a profile if $\log(\sigma_r/\sigma_t) = -0.06$, i.e., $\sigma_r/\sigma_t \approx 0.87$ (cf. Figure 3). This model is close to isotropic, but has mild tangential anisotropy. Like the isotropic model, it has an approximately constant mass-to-number-density ratio (cf. Figure 4). The logarithmic slope of $\rho(r)$ at the last data point ($R = 1.5$) equals 2.7. So even though this model is consistent with an NFW profile, the data do not actually allow us to test whether the mass density slope converges to 3 at large radii, as in the NFW profile. Figure 3 shows that the model with $\log(\sigma_r/\sigma_t) = -0.06$ has scale length $a = 0.24$ (as

⁴Efstathiou, Ellis, & Carter (1980) studied the case of test-particles with number density $\nu(r) \propto r^{-3}$ in a spherical isothermal potential. The enclosed mass $M(r)$ is then strictly independent of β for all radii. The present result is different in that $M(r)$ for the models studied here does depend strongly on β for $r \ll r_{200}$ and $r \gg r_{200}$, but not for $r \approx r_{200}$.

before, in units of r_{200}). This is in excellent agreement with the predictions of NFW’s cosmological simulations, which predict $a = 0.20$ for an $\Omega = 0.2$ open cold dark matter model and $a = 0.26$ for a flat $\Omega = 0.2$ model (cf. C97c). The Jeans modeling therefore shows that the CNOC1 data are consistent with both an NFW mass density profile and a constant mass-to-number-density ratio for clusters of galaxies, but only if the unknown velocity dispersion anisotropy has a particular value that is close to isotropic. Figures 2 and 4 show that models with other properties can fit the data equally well. To break this degeneracy we proceed with a more sophisticated analysis that uses the entire (R, v) dataset, instead of just the projected velocity dispersion profile.

3. Distribution function models

3.1. Model calculation

To interpret the velocities of individual galaxies in the CNOC1 ensemble cluster we need to construct models based on phase space distribution functions (DFs)⁵. As before, we restrict ourselves to models with constant anisotropy β . For each β , we fix the three-dimensional galaxy number density $\nu(r)$ and mass density $\rho(r)$ to those calculated in §2 from the Jeans models. Fixing the anisotropy β does not uniquely determine the DF. For given $\nu(r)$ and $\rho(r)$ there are infinitely many DFs that all predict the same second order velocity moments; a DF is determined uniquely only after specification of all its velocity moments (e.g., Dejonghe 1986). Here we do not seek to derive the full set of DFs that can generate a model with a given anisotropy, but instead we are satisfied to find just one. To achieve this we make a simple ansatz for the DF: $f = f_\beta(E, L) \equiv g_\beta(E)L^{-2\beta}$, where E and L are the binding energy and angular momentum per unit mass. Such models have fixed constant anisotropy β (e.g., Hénon 1973; Kent & Gunn 1982; Cuddeford 1991). The problem lies in finding the function $g_\beta(E)$ that generates the required $\nu(r)$ in the given $\rho(r)$. The number-density profile is given by

$$\nu(r) \equiv \int f(E, L) d^3\underline{v} = 2^{3/2-\beta} \pi^{3/2} r^{-2\beta} \frac{\Gamma(1-\beta)}{\Gamma(\frac{3}{2}-\beta)} \int_0^{\psi(r)} g_\beta(E) [\psi(r) - E]^{1/2-\beta} dE. \quad (4)$$

Here $\psi(r) = E - \frac{1}{2}v^2$ is the relative gravitational potential, which is uniquely determined by the mass density distribution $\rho(r)$ through Poisson’s equation (e.g., Binney & Tremaine 1987).

For each fixed value of β we solve equation (4) for $g_\beta(E)$ using the penalized likelihood method described in Appendix C of Magorrian & Tremaine (1999). This generally yields a solution for which the predicted $\nu(r)$ agrees to within $\lesssim 1\%$ with the $\nu(r)$ inferred from the data. Only for radially anisotropic models with $\sigma_r/\sigma_t \gtrsim 2$ could we not achieve such good agreement. This

⁵Ramirez & De Souza (1998) and Ramirez, De Souza & Schade (1999) bypassed the calculation of DFs in their modeling of the projected velocity distributions of clusters by making a number of simplifying assumptions, and they used the resulting kinematic models to draw conclusions about the velocity dispersion anisotropy of cluster galaxies of different morphological types. Appendix A presents a quantitative assesment of the validity of their approach and conclusions.

is not due to a numerical flaw in our approach, but indicates that such radially anisotropic DFs cannot produce central density cusps that are as shallow as observed (Figure 1). This by itself can be taken as evidence against these models. However, the models fail only at radii $r \lesssim 0.1$, where the constraints from the data are not very strong (due to small-number statistics). Because of this, we have not excluded radially anisotropic models with $\sigma_r/\sigma_t \gtrsim 2$ from our analysis. Instead we use for them the best, albeit imperfect, solution to equation (4). This has little impact on our final conclusions, because as we will show below, even more mildly radially anisotropic models are already strongly ruled out by the data.

Once the DF has been calculated, we are interested in the probability $\mathcal{F}_\beta(R, v) dv$ that a particle observed at projected radius R is observed to have line-of-sight velocity v between v and $v + dv$. This probability is given by an integral over the DF:

$$\mathcal{F}_\beta(R, v) = \frac{1}{\Sigma(R)} \int dz \iint dv_x dv_y f_\beta(E, L), \quad (5)$$

where (x, y, z) is a cartesian coordinate system with the z -axis along the line of sight (i.e., the line-of-sight velocity v equals v_z). For the numerical evaluation of the outer, line-of-sight, integral we change variables from z to $u \equiv \text{arsinh}(z/R)$. The evaluation of the inner integral over (v_x, v_y) is more complicated. We transform to polar co-ordinates (w, ζ) defined by $v_x \equiv w \cos \zeta$ and $v_y \equiv w \sin \zeta$. For models with $\beta \leq 0$ we directly evaluate the resulting double integral over (w, ζ) . Models with $\beta > 0$, however, have an awkward singularity in the DF at $L = 0$. For these models we apply an additional change of variables from ζ to $s \equiv \ln \tan \frac{1}{2}\zeta$.

3.2. Data-model comparison

We used the approach of §3.1 to calculate the DFs and probability distributions $\mathcal{F}_\beta(R, v)$ for each of the eleven constant- β models shown in Figure 3. With these models we study the (R, v) datapoints in the CNOC1 cluster survey for those galaxies with K-corrected absolute Gunn r -band magnitude $M_r < -18.5$. Galaxies in the clusters MS 0906+11 and MS 1358+62 were excluded; these clusters are strong binaries for which spherical models cannot be appropriate (C97b). The sample of galaxies from the remaining 14 survey clusters was restricted to those galaxies with $R \leq 1.5$ and $|v| \leq v_{\text{max}} \equiv 4$. So, without loss of generality, we ignore the regions of (R, v) space where cluster members are scarce among large numbers of interlopers. The remaining sample contains 990 galaxies.

The sample thus defined is still expected to contain interlopers. We have not attempted any identification and removal of individual interlopers, but instead take interloper contamination into account in a statistical sense. We assume: (i) that the density of interlopers at fixed R is homogeneous in v ; and (ii) that the probability f_i for a galaxy at known R but unknown v to be an interloper is independent of R . With these assumptions, f_i is the total fraction of interlopers in the sample. While this treatment of interlopers was motivated in part by mathematical simplicity, it does not oversimplify things to the point where the models become inadequate. We discuss the merits and limitations of our treatment of interlopers in detail in §4.1 below.

3.2.1. Likelihood analysis

Let galaxy number j in the sample be observed at radius R_j . The probability $\mathcal{F}(R_j, v)dv$ that the observed velocity v of the galaxy falls between v and $v + dv$ is given by

$$\mathcal{F}(R_j, v)dv = \begin{cases} f_i (dv/2v_{\max}) + (1 - f_i) \hat{\mathcal{F}}_\beta(R_j, v)dv, & |v| \leq v_{\max} ; \\ 0, & |v| > v_{\max} . \end{cases} \quad (6)$$

In this equation $\hat{\mathcal{F}}_\beta(R_j, v)$ denotes the convolution of $\mathcal{F}_\beta(R_j, v)$ with a normalized Gaussian of dispersion Δv_j , where Δv_j is the formal measurement error in the determination of the velocity v_j of galaxy j . The velocity errors are typically $\lesssim 140 \text{ km s}^{-1}$, or $|\Delta v_j| \lesssim 0.15$ in dimensionless units (small enough to have negligible influence on any part of our analysis). The probability $\mathcal{F}(R_j, v)$ in equation (6) is normalized to unity, since realistic dynamical models predict $\mathcal{F}_\beta(R, v) \approx 0$ for $|v| > v_{\max} = 4$.

The complete dataset consists of N galaxies observed at (R_j, v_j) , with $j = 1, \dots, N$. The probability of this dataset in a given cluster model is proportional to the likelihood $L \equiv \prod_{j=1}^N \mathcal{F}(R_j, v_j)$. Instead of maximizing the likelihood we seek to minimize the quantity⁶

$$\lambda \equiv -2 \ln L = -2 \sum_{j=1}^N \ln[\mathcal{F}(R_j, v_j)]. \quad (7)$$

The goal is to calculate the likelihood quantity λ on a grid of the model parameters (β, f_i) , and to search for the best-fitting model that yields the minimum value λ_{\min} . Two further questions then remain to be answered: (a) is the best-fitting model statistically acceptable; and (b) what are the confidence regions around the best-fitting model parameters? To address the first question we resort to Monte-Carlo simulations. For each galaxy j in the sample we draw a velocity from the probability distribution $\mathcal{F}(R_j, v)$ for the best-fitting model. For the resulting pseudo-dataset we calculate the likelihood quantity λ as defined by equation (7). This is repeated many times. From the resulting set of λ values we calculate the median, as well as the confidences region around the median that contain a fixed fraction of the simulated λ values (e.g., 68.3%, which corresponds to 1- σ for a Gaussian distribution, or 95.4% which corresponds to 2- σ). To address the second question and obtain confidence regions around the best-fitting model parameters, we use a well-known theorem of mathematical statistics (e.g., Stuart & Ord 1991; used also by Merritt & Saha 1993): the likelihood-ratio statistic $\lambda - \lambda_{\min}$ tends to a χ^2 statistic in the limit of $N \rightarrow \infty$, with the number of degrees-of-freedom equal to the number of free parameters that have not yet been varied and chosen so as to optimize the fit. Hence, the likelihood-ratio statistic $\lambda - \lambda_{\min}$ reduces to the well-known $\Delta\chi^2$ statistic (e.g., Press et al. 1992) for $N \rightarrow \infty$, despite the fact that the $\mathcal{F}(R_j, v)$ are not individually Gaussian. This is a consequence of the central limit theorem. In principle it would be more robust to calculate the confidence regions on the best-fitting model parameters (β, f_i) by means of Monte-Carlo simulation (or, e.g., bootstrapping), but in the present context this was found to be prohibitively expensive computationally.

⁶In an ideal case in which the $\mathcal{F}(R_j, v)$ are all Gaussian (not true here), λ reduces to a χ^2 statistic.

Figure 5 shows the interloper fraction f_i that minimizes λ as a function of anisotropy, with $1\text{-}\sigma$ error bars calculated as described above. The figure shows that f_i is in the range $f_i = 0.115 \pm 0.02$ for all anisotropies studied, with a formal error of ± 0.02 at fixed anisotropy. In the remainder of the paper we always use, for each given anisotropy, the optimal f_i shown in Figure 5. Figure 6 shows λ as function of the velocity dispersion anisotropy. The overall minimum is $\lambda_{\min} = 1783.1$ for the model with $\sigma_r/\sigma_t = 0.92$ (i.e., not far from isotropic). Monte-Carlo drawing from this model yields a predicted $\lambda = 1766.9 \pm 48.6$ with 68.3% confidence; hence, the observed likelihood is acceptable. Confidence boundaries on the best-fitting σ_r/σ_t as obtained from the likelihood ratio statistic $\lambda - \lambda_{\min}$ are indicated in the figure. At 68.3% confidence $0.80 \leq \sigma_r/\sigma_t \leq 1.01$ and at 95.4% confidence $0.48 \leq \sigma_r/\sigma_t \leq 1.11$.

The structural properties of the ensemble cluster depend on σ_r/σ_t , as shown in Figures 3 and 4. The inner slope ξ and scale length a of the mass density, and also the mass-to-number density ratio ρ/ν , are of particular interest. Our methods do not directly allow us to obtain confidence intervals on these quantities. However, approximate confidence intervals are obtained by determining how ξ , a and ρ/ν vary in Figures 3 and 4 when σ_r/σ_t is varied over, e.g., its 68.3% confidence range. This yields $0.70 \leq \xi \leq 1.13$, $0.23 \leq a \leq 0.27$, and over the radial range $0.1 \leq R \leq 1$, $0.47 \leq \log(\rho/\nu) \leq 0.65$. The data are therefore consistent with an NFW profile and with a mass-to-number density ratio that is constant to within $\sim 25\%$ over the radial range $0.1 \leq R \leq 1$, both at 68.3% confidence.

3.2.2. Grand-total velocity histogram

The likelihood is only one of many statistics that one can use to test the validity of a model. There are several reasons why it is useful to quantitatively consider other statistics as well. First, other statistics will be sensitive to different aspects of the data, and can therefore yield different estimates of the best model and different (possibly smaller) confidence regions. Second, there is no guarantee that any of our models actually provides an adequate representation of the DF that underlies the data (e.g., the ensemble cluster may not be perfectly spherical or have non-constant β). While the likelihood suggests that the best-fit model of §3.2.1 is statistically acceptable, other statistics may well indicate that none of our models are acceptable. Third, the likelihood analysis shows that some of our models are more likely than others, despite the fact that all models fit the projected velocity dispersion profile equally well. The likelihood provides little insight into *why* this is the case, and other statistics may do a better job in this respect. Based on these arguments we have considered some other statistics that address the properties of the grand-total velocity histogram for the ensemble cluster.

The grand-total velocity distribution predicted by a given model is simply:

$$\mathcal{F}_{\text{tot}}(v) = \frac{1}{N} \sum_{j=1}^N \mathcal{F}(R_j, v), \quad (8)$$

where $\mathcal{F}(R_j, v)$ is given by equation (6). However, this method of calculating the predicted velocity distribution for a model provides no insight into the random fluctuations caused by the

shot noise. The observed grand-total velocity histogram is determined by a finite number of galaxies, and this is best simulated in Monte-Carlo manner. For each model with given anisotropy we therefore draw velocities from the probability distributions $\mathcal{F}(R_j, v)$ for each of the N galaxies in the sample, which yields a simulated grand-total velocity histogram. This procedure is repeated many times, and for each histogram bin we calculate the median occupation of the bin, and the range around the median that contains the occupation value for 68.3% of the simulations.

Figure 7 shows the predicted, normalized grand-total velocity histograms as function of $|v|$ for three constant- β models. In each panel the predictions are shown as a combination of two thin lines; for each bin, the histogram occupation falls between these lines in 68.3% of the simulations. The thick line in each of the panels is the observed velocity histogram. The predicted velocity histogram is approximately Gaussian for the isotropic model; it is more flat-topped than a Gaussian for tangentially anisotropic models, and more centrally peaked than a Gaussian for radially anisotropic models. These results are consistent with previous calculations (in other contexts) of the velocity distributions predicted by constant anisotropy models (e.g., Merritt 1987; van der Marel & Franx 1993). The observed histogram is neither particularly centrally peaked nor particularly flat-topped, and this is why the likelihood analysis of §3.2.1 yields a best-fit model that is close to isotropic.

One method to address whether the differences between the observed and predicted grand-total velocity histograms are statistically acceptable is through a χ^2 quantity that sums the squared residuals over all bins of the velocity histogram, weighted with the shot-noise errors predicted from the Monte-Carlo simulations. We calculated this quantity, and found a minimum $\chi^2 = 26.1$ for the model with $\sigma_r/\sigma_t = 0.91$. The expected value with 20 velocity bins is $\chi^2 = 20.0 \pm 6.6$ at 68.3% confidence, suggesting that the best fit model is acceptable. Confidence boundaries on σ_r/σ_t were calculated from the usual $\Delta\chi^2$ statistic, yielding $0.74 \leq \sigma_r/\sigma_t \leq 1.02$ at 68.3% confidence and $0.47 \leq \sigma_r/\sigma_t \leq 1.13$ at 95.4% confidence. These results are virtually identical to those derived in §3.2.1 from the likelihood statistic λ . Apparently, little information is lost by putting all datapoints together in one grand-total velocity histogram (which removes information on radial dependencies).

More insight can be gained by considering statistics that address the *shape* of the grand-total velocity histogram. By construction, the predicted histograms for models with different β are all normalized, and have the same dispersion. The most obvious shape statistics are therefore the kurtosis and other higher order moments (Stuart & Ord 1991). However, these moments are very sensitive to the wings of the velocity distribution, which are not particularly well constrained (primarily due to interlopers). The Gauss-Hermite moments provide more suitable statistics, since they are by construction insensitive to the wings of the distribution (van der Marel & Franx 1993; Gerhard 1993). These moments have been used before to describe cluster velocity histograms, but primarily as a method for searching for cluster substructure (Zabludoff et al. 1993; see also Colless & Dunn 1996).

To calculate the Gauss-Hermite moments for the CNOC1 ensemble cluster, the observed velocities were binned into a grand-total histogram $\mathcal{F}_{\text{tot,observed}}(v)$ as in Figure 7. The estimated

contribution by interlopers was then subtracted to yield a corrected histogram:

$$\mathcal{F}_{\text{tot,corrected}}(v) = [\mathcal{F}_{\text{tot,observed}}(v) - (f_i/2v_{\text{max}})] / (1 - f_i), \quad |v| \leq v_{\text{max}}. \quad (9)$$

From this corrected histogram we calculated the two lowest order non-trivial Gauss-Hermite moments⁷, namely h_4 and h_6 . The resulting moments were found to be independent of the choice of the bin size in the histogram construction⁸; hence they are well defined quantities. The best estimate for f_i depends slightly on the assumed anisotropy (cf. Figure 5), so the inferred h_4 and h_6 do so as well. This is seen in Figure 8, in which dashed curves show the dependence of the observed h_4 and h_6 on the assumed anisotropy. However, the dependence on anisotropy is small, and we find that h_4 and h_6 are in the range $h_4 = -0.015 \pm 0.005$ and $h_6 = -0.028 \pm 0.006$ for all anisotropies that we have studied.

We also calculated h_4 and h_6 for the models. As before, velocity histograms were drawn from each model in Monte-Carlo fashion. For each ensemble of simulated histograms we calculated the median and 68.3% confidence interval on h_4 and h_6 . The resulting predictions are shown in Figure 5 as solid dots with error bars. In essence, the dots are the Gauss-Hermite moments predicted for the hypothetical case in which complete information on the velocity distribution were available at the radius of each galaxy in the sample. The error bars show the 1- σ shot noise variations on these values due to the fact that only a discrete realization of the model is available with a finite number of galaxies⁹. These errors are $|\Delta h_l| \approx 0.02\text{--}0.03$, independent of either β or the Gauss-Hermite order l ¹⁰.

The tangentially anisotropic models predict flat-topped velocity histograms, which have $h_4 < 0$ and $h_6 > 0$; the radially anisotropic models predict centrally peaked velocity histograms, which have $h_4 > 0$ and $h_6 < 0$. There is generally more power in the fourth-order term than the sixth-order term. Even higher-order moments are not particularly useful in the present context, since all models that we have studied predict $h_l \approx 0$ to within the variations expected from shot noise, for all $l \geq 8$. The near-zero observed values of h_4 and h_6 are reproduced only by models that are close to isotropic. The observed values fall inside the 68.3% confidence interval for both h_4

⁷The best-fitting Gaussian is used to generate the Gauss-Hermite basis, so by definition $h_0 = 1$ and $h_2 = 0$. The odd moments are all zero for a symmetrical distribution.

⁸The underlying reason for this is that each Gauss-Hermite moment is sensitive to features in the velocity distribution on a particular characteristic velocity scale. This scale becomes finer for moments of higher order, as in a Fourier decomposition (Gerhard 1993). We find that velocity binning has no influence on the calculated moments, as long as the bin size of the histogram is smaller than the characteristic velocity scale for the highest order considered, h_6 in this case.

⁹In the approach of Figure 8, the observed Gauss-Hermite moments are fixed numbers without error bars (they are well defined integrals over the observed histogram), while the model predictions for the observed values have a shot-noise error. An alternative view is to think of the observed Gauss-Hermite moments as estimates of the moments of the underlying distribution. In this view, the models predict a fixed value (the dots in the figure), and the Monte-Carlo calculated shot-noise errors should be thought of as the errors on the observed values.

¹⁰The fact that the shot-noise errors are independent of the Gauss-Hermite order is due to the fact that the Gauss-Hermite functions form an orthonormal basis.

and h_6 if $1.00 \leq \sigma_r/\sigma_t \leq 1.05$. They fall inside the 95.4% confidence interval for both h_4 and h_6 if $0.75 \leq \sigma_r/\sigma_t \leq 1.21$. These results are broadly consistent with those derived in §3.2.1 and §3.2.2, but not entirely. In particular, tangentially anisotropic models are ruled out at higher confidence by h_4 and h_6 than they are by the likelihood statistic λ .

4. Possible uncertainties and additional considerations

The dynamical analysis in the preceding sections has yielded several interesting conclusions about the structure of clusters of galaxies. Although the analysis has been significantly more detailed than many previous studies for this and other data sets, it still involves a number of simplifying assumptions. The present section discusses how the approximations in the analysis may have affected the conclusions, and how robust the conclusions are in view of this.

4.1. Treatment of interlopers

Our sample definition assumes that cluster members have $|v| \leq v_{\max} = 4$ in units of the cluster dispersion. So we identify all galaxies with observed velocities in excess of this limit as interlopers, similar to the approach adopted by Yahil & Vidal (1977) (they use $v_{\max} = 3$). Other than this very conservative cut, no removal of interlopers from the sample is attempted. This approach differs from that used by most authors who have modeled the dynamics of clusters of galaxies. Fairly complex schemes have recently been developed for the identification of interlopers, with estimated success rates of up to 90% (e.g., Perea, del Omo & Moles 1990; den Hartog & Katgert 1996). These schemes generally rely on mass estimates obtained with specific assumptions about the orbital structure. In the present context the orbital structure is what we hope to determine, so use of these schemes could possibly introduce subtle biases. Although the schemes are tailored to be robust and conservative, we feel it is safer in the present context to model the presence of interlopers in a statistical sense, rather than to try to remove them. Note that this modeling would still be necessary even if we did try to remove interlopers, because no interloper identification scheme can be 100% successful.

In our statistical treatment of interlopers we assumed that the density of interlopers is homogeneous in velocity.¹¹ This assumption is directly verifiable, since the density of interlopers at velocities $|v| > v_{\max}$ can be determined from the CNOC1 dataset. To this end we extracted from the CNOC1 survey as before the galaxies with K-corrected absolute Gunn r -band magnitude $M_r < -18.5$, with exclusion of galaxies in the clusters MS 0906+11 and MS 1358+62. From the resulting sample we calculated the density of galaxies in (R, v) space over the region defined by

¹¹Note that we are not assuming that the *probability* for a galaxy to be an interloper is independent of v . Interlopers are assumed to have a homogeneous density in v , while cluster members have a density that increases strongly towards $|v| = 0$ (see Figure 7). Hence, the probability for a galaxy to be an interloper is a strongly increasing function of $|v|$.

$R \leq 1.5$ and $5 \leq |v| \leq 10$,¹² and also over the region defined by $R \leq 1.5$ and $|v| \leq v_{\max} = 4$. Comparison of these densities yields a direct estimate of the interloper fraction f_i for the sample studied in §3. This approach yields $f_i = 0.117$, fully consistent with the values inferred from the likelihood analysis shown in Figure 5 (the best-fitting model identified by Figure 6 has $f_i = 0.108 \pm 0.017$). This provides direct evidence that the density of interlopers is similar for $|v| \leq v_{\max} = 4$ as for $5 \leq |v| \leq 10$, thus supporting the assumption underlying our analysis. This should also serve as a warning for interloper removal schemes, which can never identify interlopers with small velocities.

The second assumption in our analysis is that the probability f_i for a galaxy at known R but unknown v to be an interloper is independent of R . This appears somewhat counter-intuitive, since the surface density $\Sigma(R)$ of cluster members is strongly peaked towards $R = 0$. So if the surface density of interlopers $\Sigma_{\text{int}}(R)$ is homogeneous, one would expect f_i to decrease towards $R = 0$ approximately as $f_i \propto [\Sigma(R)]^{-1}$. By contrast, our assumption implies $\Sigma_{\text{int}}(R) \propto \Sigma(R)$, i.e., that the density of interlopers (with $|v| \leq v_{\max} = 4$) increases as steeply towards $R = 0$ as does the density of cluster members. This may not necessarily be incorrect, because matter not belonging to the cluster may in fact be strongly clustered towards it. To address the validity of our assumption we have taken an empirical approach, by dividing the sample of §3 in two equally sized subsamples of galaxies at small and large R , respectively. The first subsample contains galaxies with $R \leq 0.41$, and has a median radius $R_{\text{med},1} = 0.23$; the second subsample contains galaxies with $0.42 \leq R \leq 1.5$, and has a median radius $R_{\text{med},2} = 0.73$. For each subsample we redid the likelihood analysis, using an isotropic model. This yields interloper fractions $f_{i,1} = 0.083 \pm 0.024$ for the first subsample, and $f_{i,2} = 0.125 \pm 0.025$ for the second subsample. So f_i does appear to decrease with decreasing radius, but this is barely significant at the $1\text{-}\sigma$ level. However, $\Sigma(R_{\text{med},1})$ is ~ 5 times as large as $\Sigma(R_{\text{med},2})$, so f_i certainly does not decrease towards $R = 0$ as fast as predicted if $\Sigma_{\text{int}}(R)$ were independent of R . So although our assumption may not be fully correct, it does seem acceptable.

All in all, none of the tests that we have done has given us reason to believe that our treatment of interlopers is significantly in error. Also, interlopers make up only a small fraction ($\sim 11\%$) of the sample studied in §3, and we do not expect the final results to be particularly sensitive to their treatment.

4.2. Choice of distribution functions

There are several restrictions to the dynamical analysis that we have employed. Although we construct phase-space distribution functions and model the full CNOC1 (R, v) dataset, we do restrict ourselves to a specific set of models. We study only models with constant anisotropy, and even among the DFs that generate models with constant anisotropy, we choose a particular

¹²C97b also assumed the density of interlopers to be homogeneous in velocity space (in their velocity dispersion calculations), but they used a somewhat larger velocity range, $5 \leq |v| \leq 25$, to determine the interloper density. This yields results that do not differ significantly from those obtained here.

set. Realistic systems are unlikely to have a velocity dispersion anisotropy that is independent of radius, and it is not a priori clear whether our results can provide any information on what range of such models could be acceptable.

Despite the shortcomings of our analysis, there are reasons to believe that our results may be more robust than they would otherwise seem. In a nutshell, our analysis boils down to the fact that the observed grand-total velocity histogram for the CNOC1 sample is close to Gaussian, and this is not generally expected for models that have significant velocity anisotropy. Van der Marel & Franx (1993) presented a simple method for calculating the Gauss-Hermite moments for constant- β models with various scale-free number densities and potentials. Such models show that the Gauss-Hermite moments are determined primarily by the overall velocity dispersion anisotropy, and to much smaller extent by the details of the number density profile and potential. Gerhard (1993) reached the same conclusion for models with varying β . So even though we have parameterized $\nu(r)$, $\rho(r)$ and β in our approach, it is likely that even with a more general non-parametric approach the observations would still imply a velocity distribution that is close to isotropic.

The approach that we have used shares many similarities to that used by Merritt & Saha (1993) to interpret 296 measured velocities for the Coma cluster. In particular, we follow their approach of maximizing the likelihood for the (R, v) dataset. Like us, they use a restricted parameterization for the mass profile; while they adopt a two-parameter family for the gravitational potential, we adopt a three-parameter family for the mass density. The technique of Merritt & Saha does have two important advantages over our approach: first, it makes a basis function expansion of the DF that allows fairly arbitrary anisotropy profiles; and second, it avoids binning and parameterization of the projected number density profile. On the other hand, our method expands on that of Merritt & Saha through the inclusion of explicit modeling of interloper contamination, the Monte-Carlo simulation of the dataset to estimate confidence regions and the goodness-of-fit, and the use of Gauss-Hermite moments. A hybrid version of our techniques would probably allow the most robust conclusions to be reached, but this is beyond the scope of the present paper.

4.3. Brightest Cluster Galaxies

Our analysis has included the brightest cluster galaxies (BCGs) of each of the clusters in the sample. BCGs have very special properties; they tend to be atypically bright, and they are generally found at $(R, v) \approx (0, 0)$. So it is not clear whether it is appropriate to treat them on a par with the other cluster members, as we have done. Exclusion of the BCGs from our sample would, among other things, decrease the projected number density $\Sigma(R)$ at small radii. Specification of $\Sigma(R)$ is the first step in our modeling approach, so our entire analysis would need to be repeated to determine accurately whether exclusion of the BCG's would alter the results of our dynamical models. To avoid this, we have chosen a more approximate route to address this issue. We removed the BCG's from the sample, and then recalculated the Gauss-Hermite moments of the observed grand-total velocity histogram. The BCGs tend to have $v \approx 0$, so their removal makes

the histogram more flat-topped. We find that h_4 and h_6 for the resulting sample are in the range $h_4 = -0.024 \pm 0.005$ and $h_6 = -0.022 \pm 0.006$ independent of the assumed anisotropy (which, as in Figure 8, influences the Gauss-Hermite moments through the best-fitting interloper fraction f_i). As discussed in §4.2, the Gauss-Hermite moments predicted by dynamical models depend primarily on the anisotropy, and to a much lesser extent on the number density profile. So it may be reasonable to use the theoretical relation between h_4 , h_6 and anisotropy in Figure 8, despite the fact that it was derived for a somewhat different $\Sigma(R)$. The observed estimates of h_4 and h_6 without BCGs then imply best-fitting models that are somewhat more tangentially anisotropic than those derived in §3, but only by $\Delta \log(\sigma_r/\sigma_t) = -0.03$. This change is small compared to the size of the confidence regions on the best-fitting models. Hence, the inclusion or removal of BCGs has no significant effect on the main conclusions from our analysis.

4.4. Non-sphericity

Clusters of galaxies are generally flattened. The mode of the distribution of projected axial ratios for clusters is $q \approx 0.6$, while the mode of the distribution of intrinsic axial ratios is $q \approx 0.45$ (de Theije, Katgert, & van Kampen 1995). It is important to know what this implies for the validity of our spherical modeling.

4.4.1. Grand-total velocity distribution

We consider as a simple test case axisymmetric clusters of fixed intrinsic axial ratio q , with number density profiles of the form studied by Hernquist (1990),

$$\nu(R, z) = \frac{1}{2\pi q} m^{-1} (1 + m)^{-3}, \quad m^2 \equiv R^2 + (z^2/q^2), \quad (10)$$

and constant mass-to-number density ratios $\rho/\nu = 1$. These models have scale length $a = 1$ and total mass $M = 1$. We restrict ourselves to the simplest type of axisymmetric systems, namely those in which the DF depends only on the two classical integrals of motion, $f = f(E, L_z)$. We denote by $\mathcal{F}_q(R, \eta; v; i) dv$ the probability that a star at position (R, η) in a polar coordinate system on the sky, residing in a system of axial ratio q that is viewed at inclination i , is observed to have line-of-sight velocity v between v and $v + dv$. The probability distributions \mathcal{F}_q can be conveniently calculated for two-integral models using, e.g., the method of Magorrian & Binney (1994). The grand-total velocity probability distribution for a system of given q and i is given by

$$\mathcal{F}_q(v; i) = \int \Sigma_q(R, \eta; i) \mathcal{F}_q(R, \eta; v; i) R dR d\eta \quad / \quad \int \Sigma_q(R, \eta; i) R dR d\eta, \quad (11)$$

where $\Sigma_q(R, \eta; i)$ is the projected number density obtained when the $\nu(R, z)$ given by equation (10) is viewed at the given inclination, and where the integrals extend over the two-dimensional plane of the sky. We denote by $\sigma_q(i)$ the velocity dispersion corresponding to the distribution $\mathcal{F}_q(v; i)$. We consider now the case of a large number of identical axisymmetric clusters of fixed intrinsic

axial ratio q , viewed from random viewing directions. From these clusters we build an ensemble cluster, as we have done for the CNOC1 data set. The grand-total velocity probability distribution of the ensemble cluster is given by

$$\mathcal{F}_q(\tilde{v}) = \int [\mathcal{F}_q(v/\sigma_q(i); i)/\sigma_q(i)] \sin i \, di \quad / \quad \int \sin i \, di, \quad (12)$$

where the integral is over all inclination angles $i \in [0, \pi/2]$, and where \tilde{v} is now a dimensionless velocity.

The velocity anisotropy of an $f(E, L_z)$ model with fixed axial ratio q can be characterized by the quantity

$$\langle \sigma_r/\sigma_t \rangle \equiv \left[2\langle v_r^2 \rangle / (\langle v_\phi^2 \rangle + \langle v_\theta^2 \rangle) \right]^{1/2}, \quad (13)$$

where the angle brackets denote mass-weighted averages over the system. For a spherical system with constant anisotropy, $\langle \sigma_r/\sigma_t \rangle$ reduces to the same quantity σ_r/σ_t that we have used to characterize anisotropy in, e.g., Figures 3, 5, 6 and 8. For an axisymmetric $f = f(E, L_z)$ system, $\langle \sigma_r/\sigma_t \rangle$ is determined uniquely by the axial ratio q , according to the tensor virial theorem (Binney & Tremaine 1987). For an oblate two-integral system,

$$\langle \sigma_r/\sigma_t \rangle_q = \left[\left(1 - \sqrt{1 - e^2} \frac{\arcsin e}{e} \right) / \left(\frac{1}{\sqrt{1 - e^2}} \frac{\arcsin e}{e} - 1 \right) \right]^{1/2}, \quad (14)$$

where the eccentricity is defined by $e^2 \equiv 1 - q^2$.

For several values of the axial ratio ranging from $q = 0.3$ to $q = 1$ we calculated the velocity distributions $\mathcal{F}_q(\tilde{v})$ as pertaining to an ensemble of randomly oriented clusters. In the integrals of equation (11) we included only radii $R \in [0.1; 3]$ to approximate the range of radii for which data is available in the CNOC1 data set. From each distribution we calculated the corresponding fourth-order Gauss-Hermite moments $h_{4,q}$, which describe the extent to which the distributions deviate from Gaussians, and for each axial ratio we also calculated the velocity anisotropy parameter $\langle \sigma_r/\sigma_t \rangle_q$. The dots in Figure 9 connected by a solid curve show $h_{4,q}$ as function of $\langle \sigma_r/\sigma_t \rangle_q$. For comparison, we also calculated the relation between h_4 and σ_r/σ_t for *spherical* constant- β models with a Hernquist density profile, using the approach of §3.1. Those results are shown as a dashed curve in Figure 9. The results of these two very different calculations are virtually identical.

4.4.2. Radial dependence of model quantities

Figure 9 suggests that it is reasonable to model the grand-total velocity distribution of an ensemble of axisymmetric clusters with a spherical model. However, for a spherical model to be appropriate it must also predict the correct radial dependence for all observable quantities. The projected intensity profile of an ensemble of axisymmetric clusters is given by

$$\Sigma_q(R) = \frac{1}{2\pi} \int \Sigma_q(R, \eta; i) \, d\eta \sin i \, di, \quad (15)$$

where the integrals are over $\eta \in [0, 2\pi]$ and $i \in [0, \pi/2]$. The radial profiles of the kinematical quantities are obtained by evaluating equation (11) without the integrals over $R \, dR$, followed by integration over inclinations as in equation (12). This yields velocity probability distributions from which one can calculate the run of the velocity dispersion and the Gauss-Hermite moment h_4 . We did these calculations for an ensemble of two-integral Hernquist models with axial ratio $q = 0.6$; the solid curves in Figure 10 show the resulting profiles.

We used the approach of §3.1 to calculate a constant- β DF for the spherical model that has the same projected intensity profile as the ensemble of axisymmetric clusters, with σ_r/σ_t fixed to the value $\langle \sigma_r/\sigma_t \rangle = 0.81$ that applies to an $f(E, L_z)$ model with $q = 0.6$. The dashed curves in the bottom two panels of Figure 10 show the resulting $\sigma(R)$ and $h_4(R)$. The profiles are closely similar to those for the ensemble cluster, with residuals $|\Delta \log \sigma| \lesssim 0.04$ and $|\Delta h_4| \lesssim 0.02$ at all radii of interest. The projected intensity profile of the ensemble cluster is almost identical (residuals $|\Delta \Sigma| \lesssim 0.01$) to the projected intensity profile of a spherical Hernquist model with a scale length a for which $\log a = -0.046$. This also differs only slightly from the value ($\log a = 0$) for the axisymmetric clusters from which the ensemble was constructed.

The curves for the ensemble in Figure 10 were obtained without scaling each cluster with its individual velocity dispersion $\sigma_q(i)$ in equation (12). The normalizations of $\sigma(R)$ for the ensemble cluster and the spherical model are therefore similar in an absolute sense.¹³ This is important for cluster mass determinations, since $M \propto \sigma^2$. It implies that the average mass (or mass-to-light ratio) of a set of clusters can be adequately determined from spherical models, even if the clusters are individually axisymmetric.

4.4.3. Dependence on axial ratio and anisotropy

The $f(E, L_z)$ models discussed so far provide only one possible dynamical structure for axisymmetric systems. In general, the construction of DFs for axisymmetric systems is a complicated problem (e.g., van der Marel et al. 1998; Cretton et al. 1999) that is beyond the scope of the present paper. However, if we restrict ourselves to the case of asymptotically large radii then the problem becomes more tractable. An axisymmetric Hernquist model then reduces to a scale-free spheroidal mass density in a Kepler potential. Two families of three-integral DFs for this limiting case were presented by de Bruijne et al. (1996). Each family has one free parameter called β . In the spherical limit both families reduce to the spherical constant- β models that we have discussed in §3.1, but in the more general axisymmetric case the families have different properties. The ‘case I’ DFs for a given axial ratio are generalizations of the $f(E, L_z)$ models; they reduce to the $f(E, L_z)$ model for $\beta = 0$. The ‘case II’ DFs for a given axial ratio correspond to models in which the velocity anisotropy $\beta \equiv 1 - \sigma_t^2/\sigma_r^2$ is constant throughout the system, whereas the anisotropies σ_θ/σ_r and σ_ϕ/σ_r are not. The case II DFs have a particularly interesting

¹³It was verified that the agreement between $\sigma(R)$ and $h_4(R)$ for the ensemble cluster and the spherical model does not deteriorate when one does include the scaling of clusters with their individual velocity dispersion (as we have done for the CNOC1 dataset).

property in the present context. If one constructs an ensemble of axisymmetric models with this DF, then the entire projected velocity distribution of this ensemble (i.e., the velocity dispersion and all Gauss-Hermite moments) is identical to that for a spherical model with the same β . This is true for any axial ratio q and velocity anisotropy β . So if clusters of galaxies are axisymmetric with DFs of this type, then the construction of spherical models for an ensemble of such clusters will yield *exactly* the correct results (at large radii), even for extreme axial ratios or anisotropies.

In general, the differences between the predictions of an ensemble of axisymmetric systems and a corresponding spherical model will depend on the details of the shapes and DFs of clusters of galaxies, which are not known. However, the combined results of all the tests that we have done indicate that the agreement in all quantities of interest is generally quite good. Hence, it appears adequate to use spherical models to interpret data for an ensemble of clusters that may individually not be spherical.

4.5. Homology

The CNOC1 ensemble cluster that we have analyzed was constructed under the assumption that clusters form a homologous set. This allowed us to scale all data in both radius and velocity. The virial theorem for a collisionless system states that $\sigma^2 = GM/r_g$, where σ is the grand-total velocity dispersion of the system, M is its mass, and r_g is the gravitational radius (Binney & Tremaine 1987). To properly scale the data for a homologous set of clusters, one would need to scale all velocities by σ and all radii by r_g . However, $r_g \equiv GM^2/W$ is defined in terms of the potential energy W of the system, which itself depends on the exact radial profile of the mass density (Binney & Tremaine 1987). This is what we wish to determine, and r_g is therefore not known a priori for individual clusters. Lacking knowledge of r_g , we scaled all radii with r_{200} when building the CNOC1 ensemble cluster in §2.

One may wonder whether the scaling of the data with r_{200} may have biased the results of our analysis in some way. The likely answer is that it hasn't. In §3.2.2 we compared model predictions to the grand-total CNOC1 velocity histogram. This histogram is entirely independent of the radial scaling adopted in the construction of the ensemble cluster; it only depends on the velocity scaling. Nonetheless, the results obtained from the grand-total CNOC1 velocity histogram are in good agreement with those obtained from the more complete likelihood analysis, which does depend on the details of the radial scaling adopted in the building of the ensemble cluster. This indicates that our results are robust, and not particularly sensitive to the adopted radial scaling.

The radii r_{200} for the CNOC1 clusters were calculated from the relation $r_{200} = \sqrt{3}\sigma/10H(z)$, where $H(z)$ is the Hubble constant at redshift z (C97b). To assess the influence of the radial scaling further we did some tests with ensembles of hypothetical clusters that obey a relation of the form $R \propto \sigma^\tau$ with $\tau \neq 1$. These were then analyzed under the assumption $R \propto \sigma$ that was made in the analysis of the CNOC1 data. These tests confirmed that the results of our analysis are not very sensitive to possible errors in the adopted radial scaling, for reasonable values of τ (Section 3.1 of Schaeffer et al. 1993 indicates $\tau \approx 1.15 \pm 0.3$, so the scaling adopted for the CNOC1

dataset is itself not inconsistent with the data).

There is some evidence for the fact that clusters may form a homologous set from the fact that their global properties appear to lie on a fundamental plane, as for elliptical galaxies (Schaeffer et al. 1993). However, it is still quite possible that clusters are in fact not homologous at all. If so, our results would only (at best) be valid in some average sense. For example, our conclusion that the CNOC1 ensemble cluster is consistent with an isotropic velocity distribution may well be consistent with the (contrived) hypothesis that half of the CNOC1 clusters are strongly radially anisotropic and the other half are strongly tangentially anisotropic.

The possible presence of cluster substructure may be another cause of non-homology. However, the two clusters in which substructure is most readily apparent, MS 0906+11 and MS 1358+62, were excluded from the analysis. X-ray images for the remaining clusters appear mostly regular, and dynamical and X-ray mass estimates agree well (Lewis et al. 1999); this argues against significant substructure. Also, the procedure of adding individual clusters together minimizes the effect of any possible substructure in the dynamical analysis.

5. Discussion and conclusions

In the context of the CNOC1 cluster survey, redshifts were obtained for galaxies in 16 clusters at $z = 0.17\text{--}0.55$, selected on the basis of their X-ray luminosity (e.g., C96). The resulting sample is ideally suited for an analysis of the internal velocity and mass distribution of clusters of galaxies. Previous analyses of this dataset were based on Jeans equation models for the projected velocity dispersion profile $\sigma(R)$ (C97b,c). The results of such models always have a strong degeneracy between the mass density profile $\rho(r)$ and the velocity dispersion anisotropy profile $\beta(r)$, because these two functions of one variable are only constrained by one function of one variable. Here we have attempted to break this degeneracy by analyzing not only $\sigma(R)$, but the full (R, v) dataset of the CNOC1 cluster survey. The sample consists of 990 galaxies with $R \leq 1.5$ and $|v| \leq v_{\max} = 4$ in dimensionless units.

In §2 we repeated some of the previous Jeans modeling, although with a somewhat different approach from that employed by C97b,c. The results provide an illustration of the degeneracies involved in the modeling, and serve as a useful starting point for a more detailed analysis. In §3 we presented an analysis of the full (R, v) dataset, using a one-parameter family of models with different constant velocity dispersion anisotropy, each using a different mass density profile $\rho(r)$ and providing the same acceptable fit to $\sigma(R)$. The best-fit model was sought using a variety of statistics, including the likelihood of the dataset, and the Gauss-Hermite moments of the grand-total velocity histogram. The confidence regions and goodness-of-fit for the best-fit model were determined using Monte-Carlo simulations. Although the results differ slightly depending on which statistic is used, all statistics agree that best-fit model is close to isotropic. The isotropic model is acceptable at the $1\text{-}\sigma$ confidence level for all statistics used. For none of the statistics does the $1\text{-}\sigma$ confidence region extend below $\sigma_r/\sigma_t = 0.74$, or above $\sigma_r/\sigma_t = 1.05$.

Cosmological N -body simulations for galaxy clusters generally predict velocity distributions

that are isotropic near the center, and that become somewhat radially anisotropic towards $\sim r_{200}$ (e.g., Crone et al. 1994; Cole & Lacey 1996; Ghigna et al. 1998). The maximum radial anisotropy is not large, $\sigma_r/\sigma_t \approx 1.3$. The number density weighted anisotropy over the region sampled by the CNOC1 data is $\sigma_r/\sigma_t \approx 1.1$. Although this value is only allowed by our analysis at the $2\text{-}\sigma$ level, theory and observations do seem to agree that the velocity distribution of galaxy clusters is not strongly anisotropic.

NFW have argued that dark matter halos have a universal mass density profile characterized by three main parameters: an inner power-law slope $\xi = 1$; an outer power-law slope 3; and a characteristic scale a where the profile changes from its inner to its outer slope, $a \approx 0.2\text{--}0.3$ in units of r_{200} (depending somewhat on the adopted cosmology; cf. C97c). In our models we have parameterized the cluster mass density similarly as NFW, but with ξ and a as free parameters. Models with different velocity dispersion anisotropy require very different values of ξ and a to fit the projected velocity dispersion profile. Only models that are close to isotropic have $\xi \approx 1$ (cf. Figure 3), and our analysis of the full (R, v) dataset shows that such models are in fact the only ones that provide a statistically acceptable fit to the data. Such models have $a \approx 0.24$, consistent with the predictions of NFW. For these models the logarithmic slope of $\rho(r)$ at the last data point ($R = 1.5$) is ~ 2.7 , so it cannot be established whether the mass density slope actually converges to 3 at large radii, as predicted by NFW. These models have an approximately constant mass-to-number density ratio, by contrast to the strongly anisotropic models that are inconsistent with the data (cf. Figure 3).

In §4 we have discussed a number of possible uncertainties in our analysis, including our treatment of interlopers and BCGs, our use of a restricted one-parameter family of distribution functions, our use of spherical models for what is in reality an ensemble of non-spherical clusters, and our assumption that clusters form a homologous set. The discussions and tests that we have presented on these issues have not provided us with any serious reasons to mistrust our results. Nonetheless, it remains true that there are a number of important approximations in our treatment. Until more detailed models are constructed, it will remain difficult to fully assess all implications of the assumptions in our analysis. Possibly the most important caveat in our results remains the fact that we have studied an ensemble cluster, built by co-adding data from 14 individual clusters under the assumption of homology. This has the advantage of reducing the influence of substructure and non-sphericity in individual clusters on the final dataset, but if clusters are not a homologous set, then our results will (at best) only be valid in an average sense.

To conclude, we have presented evidence that suggests that clusters of galaxies have approximately: (i) an isotropic velocity distribution; (ii) a mass density profile as predicted by NFW; and (iii) a mass-to-number density ratio that is constant with radius. At the very least, it has been shown that these properties are not inconsistent with the CNOC1 survey data. Additional weight is added to these conclusions by the fact that they are consistent with the preliminary results from a weak-lensing study of a set of 10 galaxy clusters with the Big Throughput Camera at CTIO. That study also yields mass density profiles that are well fit by the NFW parameterization and mass-to-light ratios that are approximately constant with radius (Dell’Antonio et al. 2000).

A. The accuracy of simple kinematic models for cluster velocity histograms

Ramirez & De Souza (1998) and Ramirez, de Souza & Schade (1999) recently presented an alternative method to model cluster velocity histograms. They studied a total of 21 clusters (including nine that were observed in the context of the CNOC1 survey) to constrain the orbital anisotropy of galaxies of different morphological types. The deviations of the cluster velocity histograms from Gaussians were quantified using the higher-order statistic $|u| \equiv (1/N) \sum_{j=1}^N |v_j/\sigma|$ (this can be viewed as an alternative to using the Gauss-Hermite moments or kurtosis). To interpret the observed values of $|u|$ they were compared to the predictions of a simple kinematical model that assumes that: (i) the velocity dispersions σ_r , σ_θ and σ_ϕ are constant through the system; and (ii) the velocity distribution is a (three-dimensional) Gaussian at any point in the system. These assumptions remove the laws of gravitational dynamics (both Poisson’s equation and the collisionless Boltzmann equation) from the problem, as well as any information contained in (and dependence on) the galaxy number density profile $\nu(r)$, the mass-density profile $\rho(r)$ and the projected velocity dispersion profile $\sigma(R)$. Instead, the shape of the cluster velocity histogram in these models is a simple unique function of only one parameter, σ_r/σ_t . The assumptions on which these models are based are not generally correct, but Ramirez et al. argue that they are reasonable and adequate for the problem at hand. As we will show, this is not actually the case.

The primary shortcoming of the Ramirez et al. models is the assumption of locally Gaussian velocity distributions. This is most easily seen for the case of very tangentially anisotropic models, which have large numbers of galaxies on (nearly) circular orbits. This leads to local velocity distributions that are strongly bimodal, with peaks at plus and minus the local circular velocity. Even after projection, such models often predict velocity distributions with pronounced double peaks (e.g., van der Marel & Franx 1993). This behavior of real dynamical systems is not reproduced by kinematical models that assume locally Gaussian velocity distributions. In such models the line-of-sight velocity distribution is unimodal everywhere along the line of sight, and hence the same is always true for the projected velocity distribution.

Calculations confirm these arguments and quantify the size of the errors that are introduced. As an example, we considered models for the CNOC1 ensemble cluster in which the velocity dispersion profiles $\sigma_r(r)$ and $\sigma_t(r)$ were calculated from the Jeans equations (as in §2), but in which the velocity distribution along the line-of-sight at any point in the system was incorrectly assumed to be a Gaussian (with dispersion given by the Jeans equations), instead of being calculated from a DF (as in §3). The predicted grand-total velocity histograms were calculated for different values of σ_r/σ_t , and their shapes were quantified through the Gauss-Hermite moments h_4 and h_6 (dashed curves in Figure 11). The results can be compared to those obtained with a self-consistent dynamical model based on a DF (solid curves in the same figure; same as the predictions in Figure 8). It is clear that the results obtained with the simplified analysis have little in common with the self-consistent results. The former always yields histograms that are more centrally peaked than a Gaussian ($h_4 > 0$), and only isotropic models produce histograms that are close to Gaussian ($h_4 \approx 0$). Ramirez et al. find the same general behavior. By contrast, self-consistent dynamical models predict a smooth transition from flat-topped to centrally-peaked profiles when going from tangential anisotropy to radial anisotropy. So while the data presented

by Ramirez et al. on the velocity histogram shapes for galaxies of different morphological types are very interesting and definitely worth further study, it appears that their kinematical models are insufficient to obtain reliable conclusions about orbital anisotropies.

REFERENCES

- Allen, S. W. 1998, *MNRAS*, 296, 392
- Bartelmann, M., & Narayan, R. 1995, in *Dark Matter*, Hold, S. S., & Bennett, C. L., eds., 307 (New York: AIP Press)
- Binney, J. J., & Mamon, G. A. 1982, *MNRAS*, 200, 361
- Binney, J., & Tremaine, S. 1987, *Galactic Dynamics* (Princeton: Princeton University Press)
- Byun, Y.-I., et al. 1996, *AJ*, 111, 1889
- Carlberg, R. G., Yee, H. K. C., Ellingson, E., Abraham, R., Gravel, P., Morris, S., & Pritchett, C. J. 1996, *ApJ*, 462, 32 (C96)
- Carlberg, R. G., et al. 1997a, *ApJ*, 476, L7 (C97a)
- Carlberg, R. G., Yee, H. K. C., & Ellingson, E. 1997b, *ApJ*, 478, 462 (C97b)
- Carlberg, R. G., et al. 1997c, *ApJ*, 485, L13 (C97c)
- Cole, S., & Lacey, C. 1996, *MNRAS*, 281, 716
- Colless, M., & Dunn, A. M. 1996, *ApJ*, 458, 435
- Cretton, N., de Zeeuw, P. T., van der Marel, R. P., & Rix, H.-W. 1999, *ApJS*, in press [astro-ph/9902034]
- Crone, M. M., Evrard, A. E., & Richstone, D. O. 1994, *ApJ*, 434, 402
- Cuddeford, P. 1991, *MNRAS*, 253, 414
- Dejonghe, H. 1986, *Phys. Rep.*, 133, 218
- Dell’Antonio, I., Tyson, J. A., Wittman, D. M., Bernstein, G., Smith, D., & Fischer, P. 2000, in preparation
- de Bruijne, J. H. J., van der Marel, R. P., & de Zeeuw, P. T. 1996, *MNRAS*, 282, 909
- den Hartog, R., & Katgert, P. 1996, *MNRAS*, 279, 349
- de Theije, P. A. M., Katgert, P., & van Kampen, E. 1995, *MNRAS*, 273, 30
- de Theije, P. A. M., van Kampen, E., Slijkhuis, R. G. 1998, *MNRAS*, 297, 195
- de Theije, P. A. M., van Kampen, E., Slijkhuis, R. G. 1999, submitted
- Diaferio, A. 1999, *MNRAS*, in press [astro-ph/9906331]
- Efstathiou, G., Ellis, R. S., & Carter, D. 1980, *MNRAS*, 193, 931
- Geller, M. J., Diaferio, A., & Kurtz, M. J. 1999, *ApJL*, 517, L23
- Gerhard, O. E. 1993, *MNRAS*, 265, 213
- Ghigna, S., Moore, B., Governato, F., Lake, G., Quinn, T., & Stadel, J. 1998, *MNRAS*, 300, 146
- Hénon, M. 1973, *A&A*, 24, 229
- Hernquist, L. 1990, *ApJ*, 356, 359

- Hughes, J. P. 1998, in ‘A New Vision of an Old Cluster: Untangling Coma Berenices’, Mazure, A., Casoli, F., Durret, F., & Gerbal D., eds., p. 175 (Word Scientific Publishing Company) [astro-ph/9709272]
- Katgert, P., et al. 1996, *A&A*, 310, 8
- Kent, S. M., & Gunn, J. E. 1982, *AJ*, 87, 945
- Lewis, A. D., Ellingson, E., Morris, S. L., & Carlberg, R. G. 1999, *ApJ*, 517, 587
- Lin, H., Yee, H. K. C., Carlberg, R. G., Morris, S. L., Sawicki, M., Patton, D., Wirth, G., & Shepard, C. W. 1999, *ApJ*, 518, 533
- Magorrian, J., & Binney, J. J. 1994, *MNRAS*, 271, 949
- Magorrian, J., & Tremaine, S. 1999, *MNRAS*, in press [astro-ph/9902032]
- Merritt, D. R. 1987, *ApJ*, 313, 121
- Merritt, D. R. 1993, *ApJ*, 413, 79
- Merritt, D. R., & Saha, P. 1993, 409, 75
- Natarajan, P., & Kneib, J.-P. 1996, *MNRAS*, 283, 1031
- Natarajan, P., Hjorth, J., & van Kampen, E. 1997, *MNRAS*, 286, 329
- Navarro, J. F., Frenk, C. S., & White, S. D. M. 1997, *ApJ*, 490, 493
- Perea, J., del Omo, A., & Moles, M. 1990, *A&A*, 237, 319
- Press, W. H., Teukolsky, S. A., Vetterling, W. T., & Flannery, B. P. 1992, *Numerical Recipes* (Cambridge: Cambridge University Press)
- Ramirez, A. C., & De Souza, R. E. 1998, *ApJ*, 496, 693
- Ramirez, A. C., De Souza, R. E., & Schade, D. 1999, *ApJ*, in press [astro-ph/9911443]
- Schaeffer, R., Maurogordato, S., Cappi, A., & Bernardeau, F. 1993, *MNRAS*, 263, L21
- Solanes, J. M., & Salvador-Sole, E. 1990, *A&A*, 234, 93
- Stuart, A., & Ord, J. K. 1991, *Kendall’s Advanced Theory of Statistics, Volume II*, 5th ed. (London: Edward Arnold, a division of Hodder & Stoughton)
- Yahil, A., & Vidal, N. V. 1977, *ApJ*, 214, 347
- Yee, H. K. C., Ellingson, E., Carlberg, R. G. 1996, *ApJS*, 102, 269
- van der Marel, R. P. 1994, *MNRAS*, 270, 271
- van der Marel, R. P., & Franx, M. 1993, *ApJ*, 407, 525
- van der Marel, R. P., Cretton, N., de Zeeuw, P. T., & Rix, H. W. 1998, *ApJ*, 493, 613
- Zabludoff, A. I., Franx, M., & Geller, M. J. 1993, *ApJ*, 419, 47

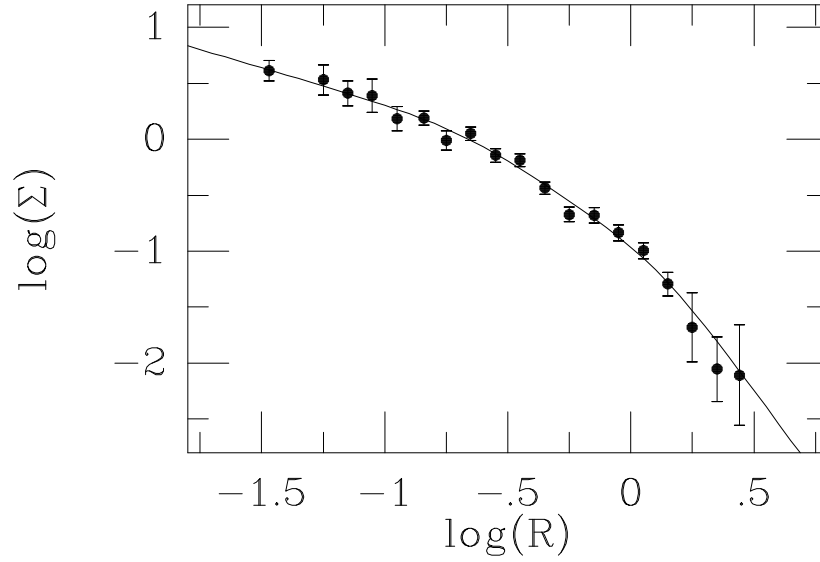


Fig. 1.— The projected galaxy number density profile $\Sigma(R)$ of the CNOC1 ensemble cluster as derived in C97b. The curve shows the parameterized fit given by equation (2), which is used in the dynamical modeling. The units along the axes are dimensionless, as described in the text.

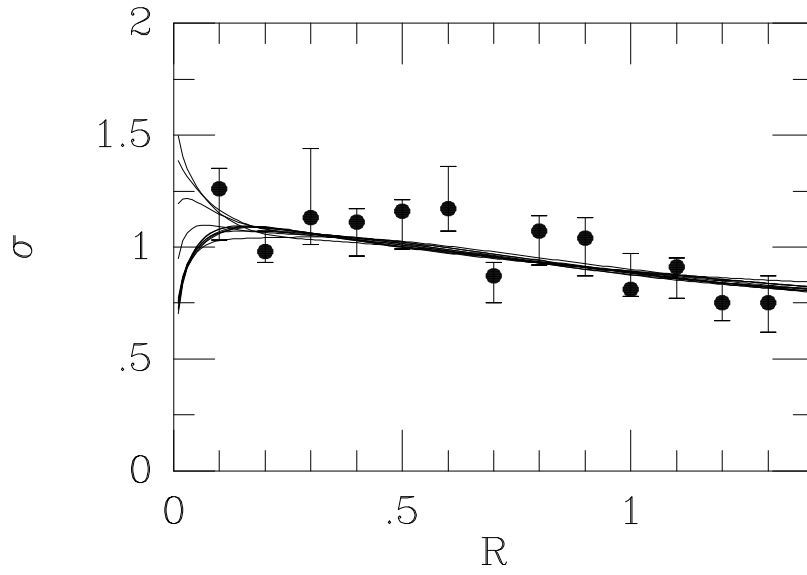


Fig. 2.— The projected velocity dispersion profile $\sigma(R)$ of the CNOC1 ensemble cluster. A 101-point running average is shown, sampled at intervals of 0.1 in the dimensionless projected radius R . The curves show the predictions of eleven models, each with different constant velocity dispersion anisotropy β . The models all provide similar, statistically acceptable fits to the data, but each uses a different mass density profile $\rho(r)$.

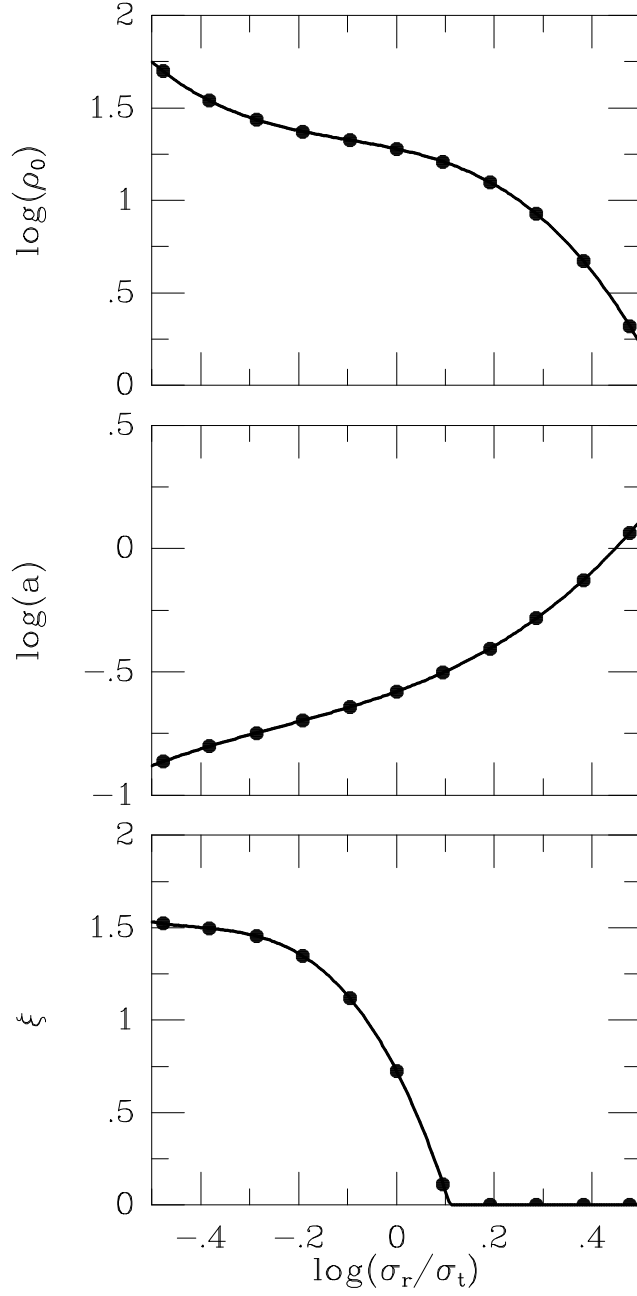


Fig. 3.— Parameters of the three-dimensional mass density $\rho(r)$ displayed in Figure 4, as function of the velocity dispersion anisotropy σ_r/σ_t , with from top to bottom: the scale density ρ_0 ; the scale radius a ; and the central power-law slope ξ . Solid dots indicate the values of σ_r/σ_t for which detailed models are constructed in this paper.

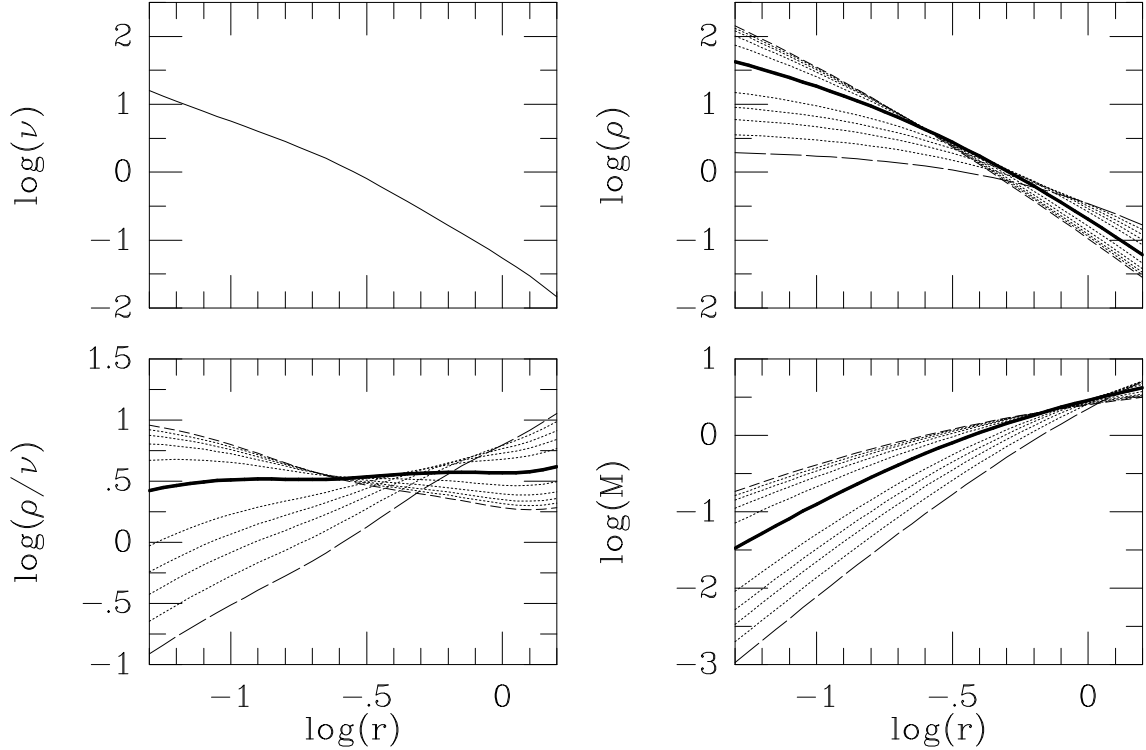


Fig. 4.— Inferred structure of the CNOC1 ensemble cluster, with from top left to bottom right: the three-dimensional galaxy number density $\nu(r)$; the three-dimensional mass density $\rho(r)$; the mass-to-number-density ratio $\rho/\nu(r)$; and the enclosed mass $M(r)$. The galaxy number density $\nu(r)$ is obtained by deprojection of the projected galaxy number density $\Sigma(R)$ shown in Figure 1. The mass density $\rho(r)$ and enclosed mass $M(r)$ are obtained by solving the Jeans equation for a spherical system so as to best fit the projected velocity dispersion profile shown in Figure 2. Eleven curves are shown, each indicating the best fit for a different constant velocity dispersion anisotropy β . The β -values of the models are logarithmically spaced in σ_r/σ_t . Heavy curves are for the best-fitting isotropic model, short dashed curves are for the best-fitting model with $\sigma_r/\sigma_t = 1/3$, and long dashed curves are for the best-fitting model with $\sigma_r/\sigma_t = 3$. The radial range shown along the abscissa corresponds approximately to the range for which the models are meaningfully constrained by the kinematical data.

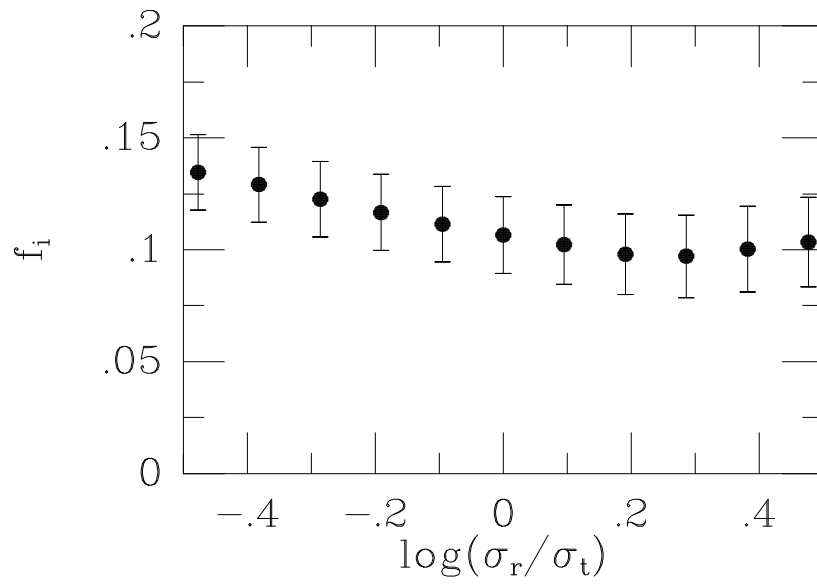


Fig. 5.— Inferred fraction f_i of interloper galaxies in the sample with 1- σ error bars, as function of the velocity dispersion anisotropy σ_r/σ_t .

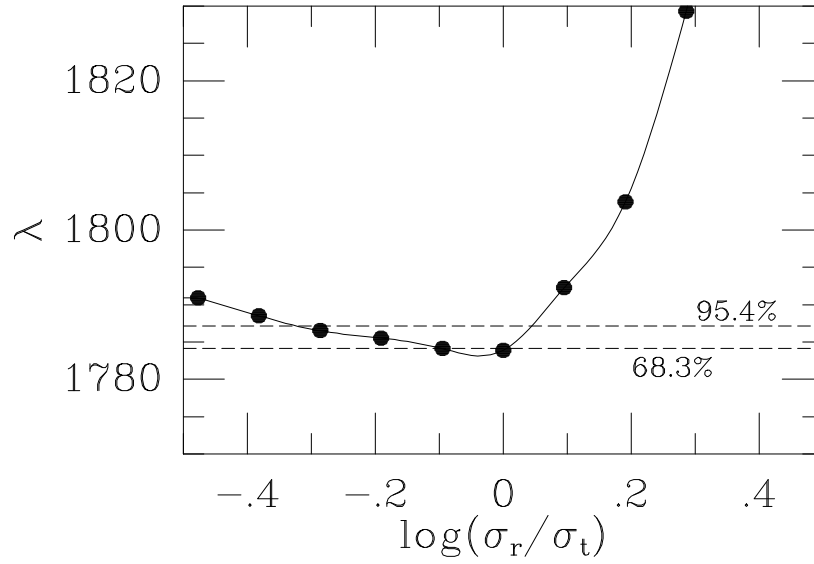


Fig. 6.— The likelihood quantity λ defined in equation (7) as function of the velocity dispersion anisotropy σ_r/σ_t . Solid points show models that were calculated; the curve is a spline fit through the points. The best fit model has $\sigma_r/\sigma_t = 0.92$, and is close to isotropic. The 68.3% and 95.4% confidence boundaries are indicated, as inferred from the likelihood-ratio statistic $\lambda - \lambda_{\min}$.

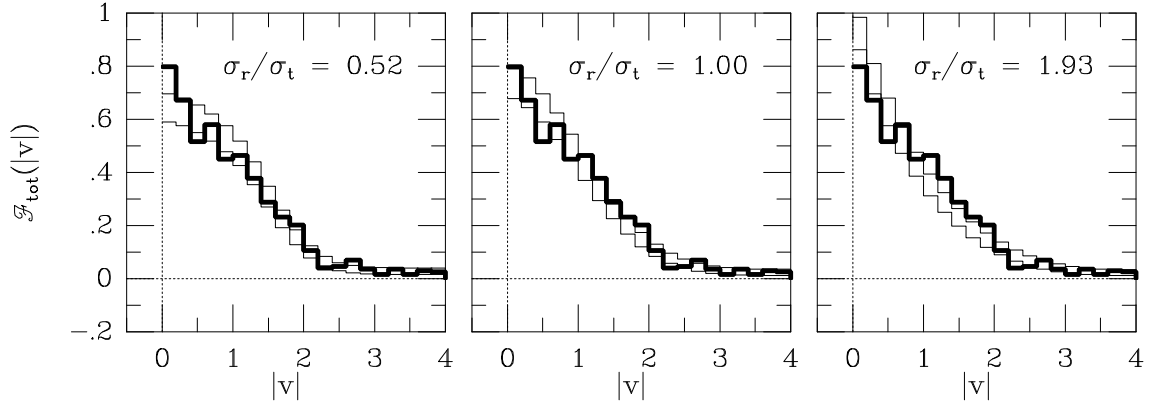


Fig. 7.— The heavy curve in each panel is the normalized grand-total velocity histogram for the CNOC1 ensemble cluster, as function of $|v|$. The regions between the two thin curves are the predictions of models with, from left to right, $\sigma_r/\sigma_t = 0.52$, 1.00 and 1.93. The model predictions take into account the shot noise due to the finite number of galaxies. In Monte-Carlo simulations the occupancy in each bin falls between the two thin curves in 68.3% of the drawings. Tangentially anisotropic models yield histograms that are more flat-topped than a Gaussian while radially anisotropic models yield histograms that are more centrally peaked. Of the models that are displayed, the isotropic model (middle panel) provides the best fit to the data.

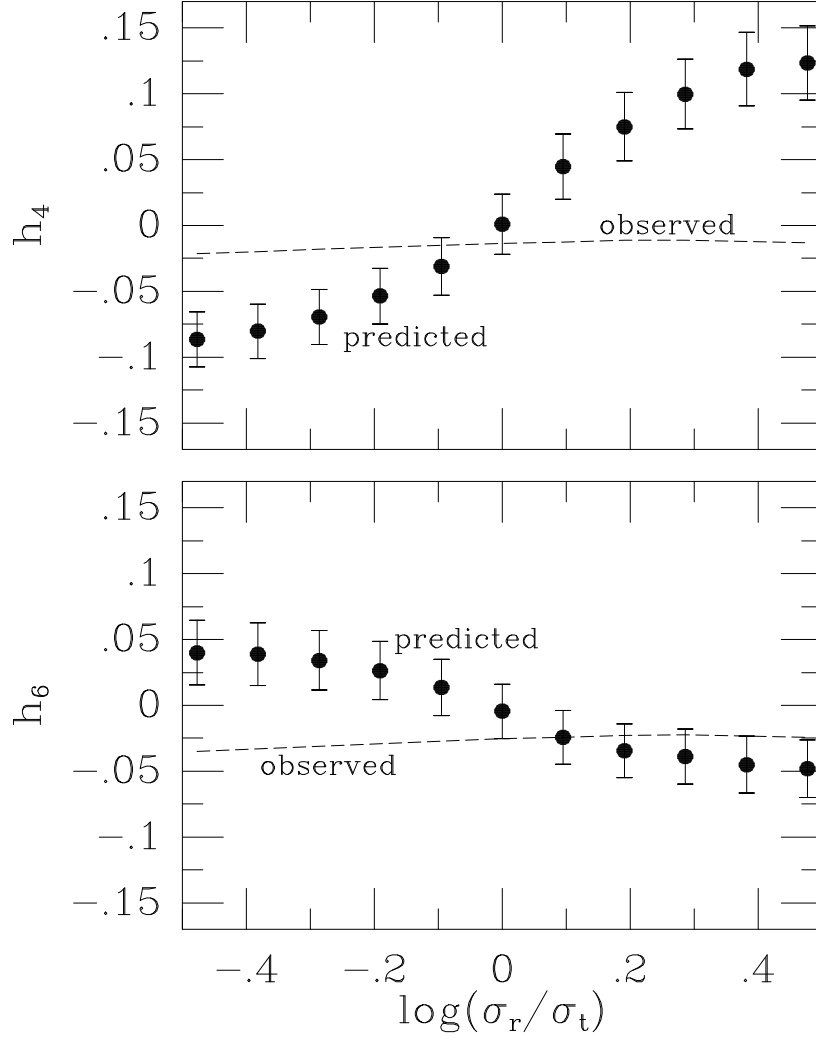


Fig. 8.— The Gauss-Hermite moments h_4 and h_6 of the grand-total velocity histogram for the CNOC1 ensemble cluster, as function of the velocity dispersion anisotropy σ_r/σ_t . The contribution from interlopers was subtracted as described in the text. The dashed curves indicate the values calculated for the observed dataset; these values depend mildly on the assumed anisotropy, because the best estimate for the fraction of interloper galaxies in the sample does. The solid points indicate the predictions of the dynamical models; the error bars are the 68.3% confidence regions calculated from Monte-Carlo simulations which take into account the finite number of galaxies in the sample. Only models that are close to isotropic provide an acceptable fit to both h_4 and h_6 .

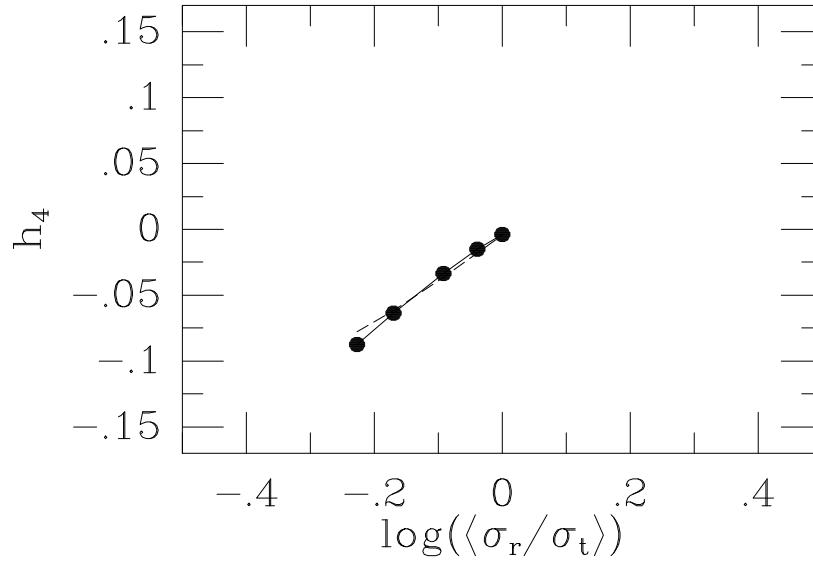


Fig. 9.— Dots connected by a solid curve are the properties calculated for an ensemble of axisymmetric two-integral Hernquist models of fixed axial ratio q , seen from random viewing directions. The Gauss-Hermite moment h_4 refers to the grand-total ensemble velocity histogram, and $\langle \sigma_r / \sigma_t \rangle$ is the velocity anisotropy defined in equation (13) in terms of mass-weighted averages over the system. The dots are for $q = 0.3, 0.4, 0.6, 0.8$ and 1.0 , from left to right respectively. For comparison, the dashed curve shows the relation between h_4 and anisotropy for spherical constant- β Hernquist models. The close similarity between the results shows that it is reasonable to use spherical models to interpret data for an ensemble of clusters that may individually not be spherical.

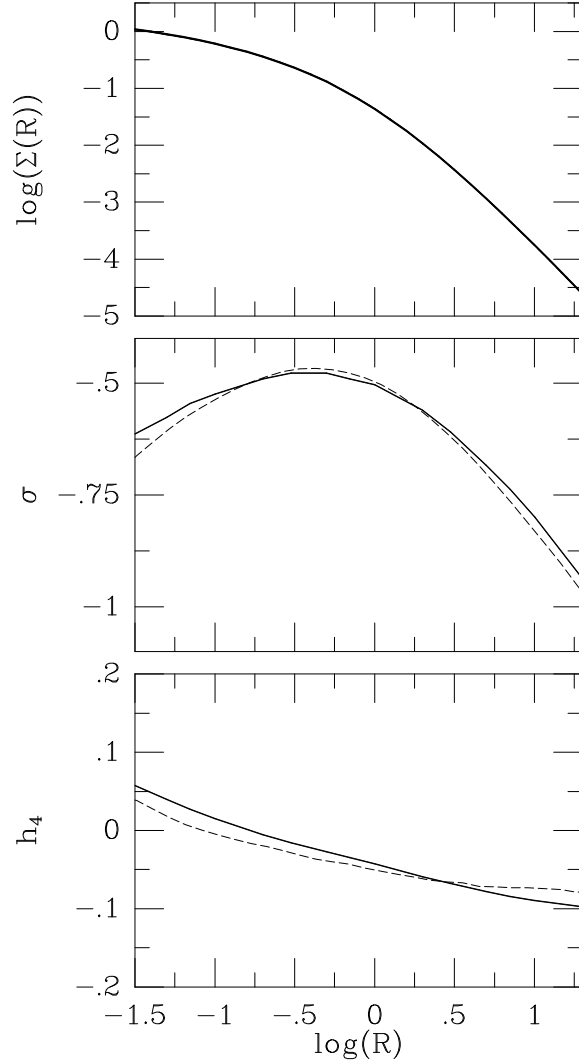


Fig. 10.— Solid curves show, from top to bottom, the projected intensity, velocity dispersion and Gauss-Hermite moment h_4 as function of radius for an ensemble of axisymmetric two-integral Hernquist models of fixed axial ratio $q = 0.6$, seen from random viewing directions. For comparison, the dashed curves in the bottom two panels show the predictions for a spherical constant- β Hernquist model with the same projected intensity profile, and the same overall anisotropy $\langle \sigma_r / \sigma_t \rangle$. The close similarity between the results shows that it is reasonable to use spherical models to interpret data for an ensemble of clusters that may individually not be spherical.

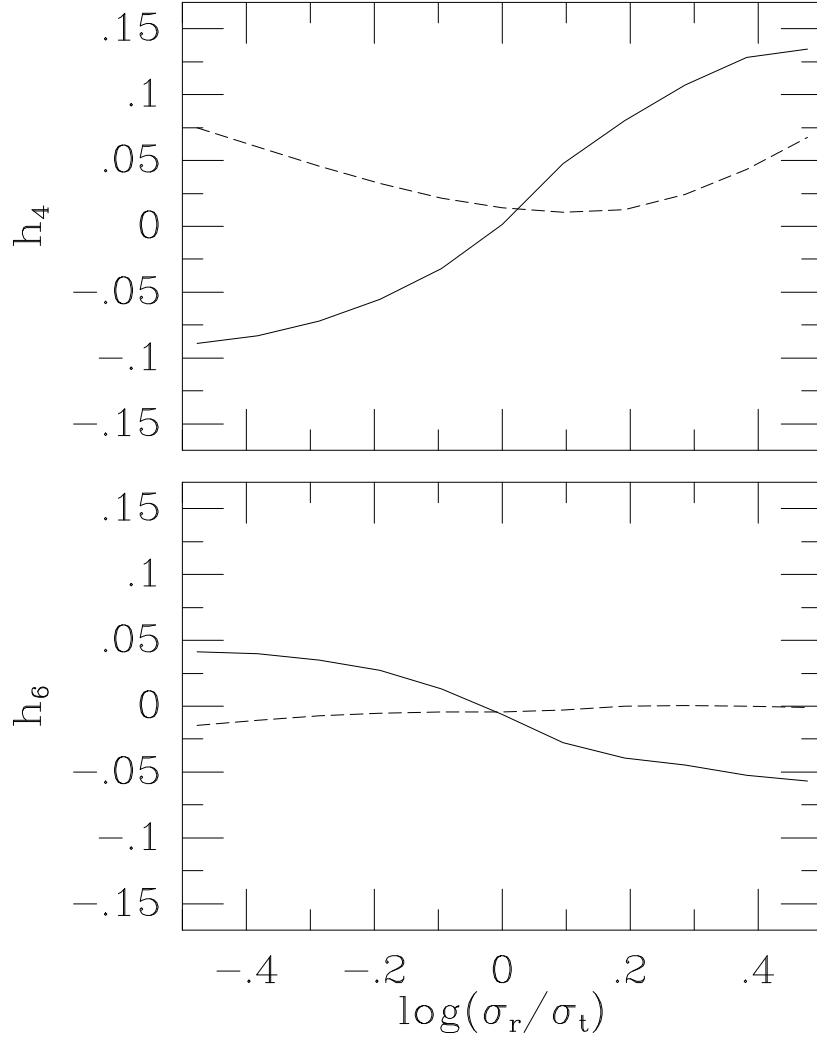


Fig. 11.— Gauss-Hermite moments h_4 and h_6 of the grand-total velocity histogram for the CNOC1 ensemble cluster, as function of the velocity dispersion anisotropy σ_r/σ_t . Solid curves show the predictions obtained with the DF modeling approach of §3 (same as the predictions in Figure 8, but without the shot-noise related error bars). Dashed curves show the predictions obtained when one incorrectly assumes that the velocity distribution is Gaussian everywhere along the line of sight, as described in Appendix A. The latter assumption, which was employed in papers by Ramirez et al., does not yield the correct results.